Yade Technical Archive
Discrete Element Method

Yade Open Source Software
March, 2018
Document Link
www.yade-doc.org

Stochastic Augmentation of the Discrete Element Method for the Investigation of Tensile Rupture in Heterogeneous Rock

Robert Caulk [1,*]

[1]University of California, San Diego, Structural Engineering, La Jolla , USA
[*]rob.caulk@gmail.com

ABSTRACT

The paper introduces a methodology designed for the investigation of rock matrix heterogeneities and their effect on pre- and post- fracture behavior. Specifically, a grain edge interaction length distribution (EILD) is constructed by Cathodoluminescnece image analysis. The EILD augments traditional Discrete Element Method (DEM) models by stochastically strengthening or weakening bonds, which simulates the presence of defects and locally tough regions. These heterogeneities cause the development of an intrinsic process zone (IPZ), which is a material property that is experimentally observable by Acoustic Emissions (AE). This paper compares the development of the IPZ within numerical and experimental three point bending tests. Similar to experimental observations, EILD-augmented DEM three point bending tests yield IPZs with variable widths. In comparison, the traditional DEM is unable to generate an IPZ. The paper concludes that the physically informed EILD contains the necessary physical distribution of grain contacts to augment DEM rock fracture models. Further analysis of the numerical AE activity reveals that larger AE events are located directly along the rupture and they are linearly related to their number of constituent interactions. As such, an AE interaction count threshold is identified to distinguish between rupture and damage AE activity. These results demonstrate the ability of the presented augmented DEM model to investigate the rock volumes associated with large rupture events for various levels of heterogeneity.

Keywords: Discrete Element Method; rock heterogeneity modeling; acoustic emission; tensile fracture; intrinsic process zone

1 Introduction

Rock fracture modeling remains challenging due to complex micromechanical processes such as the interactions of randomly oriented micro-defects, microcrack coalescence, and stochastically distributed grain-grain cementation. These micromechanical processes concentrate stress and localize strain, which result in non-linear stress-strain behaviors, large deformations, and discontinuities. Such behaviors are difficult to model, but numerous studies demonstrate the DEM-Bonded Particle Model's (BPM) (Potyondy and Cundall, 2004) ability to model emergent non-linear stress-strain behaviors at variable confining pressures (Scholtès and Donzé, 2012b; Wang and Li, 2014). Although compressive failure is well-modeled in DEM (Hazzard and Young, 2004), tensile failure models lack the experimentally observed acoustic emissions (AE) (micro failures) in the intrinsic process zone (IPZ) (Labuz et al., 1987; Lockner et al., 1992; Zietlow and Labuz, 1998) despite capturing the macroscopic rupture (Mahabadi et al., 2009). *This paper aims to demonstrate the necessity and validity of a physically constructed rock heterogeneity model for accurate simulation of AE activity during tensile rock failure in Yade DEM software.*

The study of rock heterogeneity modeling can be split into two general groups. Many studies use statistical distributions to vary material parameters, while others model some representative elementary volume (REV) of defects directly and upscale behaviors (known as homogenization). Both methods simplify the computationally intractable problem of modeling all imperfections and grain contacts within a rock specimen with the hopes of modeling the macro effect of heterogeneities: non-linear macroscopic behaviors and fracture

Suggested citation: Caulk, R. (2018) Stochastic Augmentation of the Discrete Element Method for the Investigation of Tensile Rupture in Heterogeneous Rock. *Yade Technical Archive*. DOI: 10.5281/zenodo.1202040

nucleation. DEM modelers fall into the first group; they generally represent heterogeneities by stochastically assigning micro-properties (interaction stiffness or strength properties) according to macro-property distributions (Potyondy and Cundall, 2004). Some DEM studies simply use trial and error calibration techniques to determine strength distribution mean and variation parameters (Khazaei et al., 2015; Ma and Huang, 2017). Continuum methods, such as the finite element method, approach the problem similarly by stochastically controlling the modulus parameter and failure criteria (Cai and Kaiser, 2004; Tang and Kaiser, 1998; Yang et al., 2004). Liu et al. (2004) investigated and compared a statistical approach to a direct homogenization approach. In the homogenization case, Liu et al. (2004) used microstructure image analysis to build REV material properties and geometries deterministically. In the statistical case, Liu et al. (2004) used a Weibull distribution to assign finite element strength and elastic properties. It is important to note that the Weibull distribution was characterized by a "homogeneous index", which was determined based on experimental macroscopic strength and modulus distributions. Liu et al. (2004) concluded that the statistical method closely approximated the deterministic microstructural REV method. Garboczi and Day (1995) modeled heterogeneities directly by generating model geometry based on microstructure imagery. Rabczuk and Eibl (2006) used a damage evolution model to account for heterogeneities within a meshfree concrete fracture model. Ostoja-Starzewski et al. (1994) and Buxton et al. (2001) modeled heterogeneities directly in a lattice spring model by varying spring stiffnesses depending on the solid phase that they appear in, similar to Liu et al. (2004)'s REV method. Sfantos and Aliabadi (2007) imposed heterogeneity by randomly orienting anisotropic grains in a multiscale micromechanical boundary element model. *In all aforementioned cases, heterogeneity is introduced into models by varying material parameters according to macroscopic material property distributions or modeling the microstructure directly and homogenizing the behavior at larger scales*. In comparison, the grain edge-interaction-length-distribution (EILD) presented in this paper is constructed physically by cathodoluminescence (CL) microstructure image analysis. The physically founded EILD is hypothesized to follow the same distribution of grain contact strengths, and is therefore used to stochastically control the particle interaction strengths in an augmented DEM model.

The discrepancies observed between experimental and numerical AE activity for tensile fractures indicate a gap in the micromechanical understanding of how heterogeneities affect rock behavior. Further, the well documented use of macroscopic property distributions to inform microscopic processes suggests a physically founded micromechanical method still needs to be developed for heterogeneity modeling. This study postulates that the missing piece of the traditional DEM-BPM is the lack of physically founded micromechanical material property distributions. Therefore, this paper presents an augmentation of DEM-BPM by stochastically controlling particle interaction properties according to physically founded rock grain EILD. *We hypothesize that the IPZ is controlled by the grain EILD in rocks, which can be physically constructed with CL imagery of rock grains*. This EILD augments traditional DEM by stochastically correcting the interaction areas used for bond strength assignment. In other words, the EILD-augmented DEM model accommodates naturally occurring stress concentrations as short edge (low strength, existing defects (Zietlow and Labuz, 1998)) interactions break, and long edge (locally tough regions (Alava et al., 2006)) interactions arrest and deflect fracture propagation. Several objectives are met in support of the aforementioned hypothesis. First, the paper outlines CL image analysis and EILD parameter estimation. Next, the EILD is implemented into DEM, where the IPZ is numerically simulated for a three point bending test. Finally, literature based experimental spatial and load-based IPZ AE observations are used to validate the numerical model. Ultimately, the hypothesis is supported by a method that models the mechanical behavior of a true grain packing while maintaining the computationally tractable spatial discretization of uniform particle distributions. After model validation, we explore the effect of heterogeneity on AE magnitudes and location. Finally, we demonstrate the capacity of the augmented model by distinguishing rupture and non-rupture AE activity based on numerical AE interaction count for a range of heterogeneities.

1.1 Background

1.2 Acoustic emissions in the IPZ

Acoustic Emissions are non-destructive observations of brittle material energy release prior, during, and after material rupture. Many researchers correlate AE counts to inelastic strain rates in rocks prior to failure (Boyce et al., 1981; Lockner et al., 1992). Other studies localize AE to demonstrate clustering and material damage (Berkovits and Fang, 1995; Godin et al., 2004; Shah and Labuz, 1995; Sondergeld and Estey, 1981), and some even use AE to identify field scale fracture zones (Soma et al., 2002). Recently, the magnitudes and locations of AE have shed light on heterogeneity controlled rock failures (Lei et al., 2004). A common observation of all studies is the cloud of AE activity prior to failure, followed by a coalescence of AE at the rupture location (Yang et al., 2012; Zang et al., 1998).

The collection of AE events in modern laboratories depends on computer based detection, signal conversion, and localization (Labuz et al., 2001; Lockner, 1993). An array of piezoelectric transducers generate voltage changes that are usually sampled with frequency ranges of 100 Hz - 1 MHz. These voltage changes are time stamped and converted to displacements, which can be either inverted (Eitzen and Wadley, 1984; Shah and Labuz, 1995) or plugged into empirical relationships (McLaskey et al., 2015) to determine stress drops and event magnitudes. Additionally, the hypocenter of each event is determined by minimizing residuals of P-Wave arrival times (Lockner et al., 1992; Shearer, 2009; Zang et al., 1998).

In most cases AE activity within the transducer array are accurately localized within 2 mm, but AE hypocenters beyond the array may be inaccurate up to 20 or 30 mm (Zietlow and Labuz, 1998).

The intrinsic process zone (IPZ) is an important region defined as a damaged volume of microcracks surrounding a macrocrack at peak load. Originally, the IPZ was observed using AE by Shah and Labuz (1995) and further validated by Zietlow and Labuz (1998) and Labuz et al. (2001). Development of the IPZ is attributed to the inherent heterogeneities of geomaterials such as pre-existing microcracks, misshapen grains, and mineral imperfections (Lei et al., 2000). Each heterogeneity acts to concentrate stress and extend microcracks, yielding a release of elastic waves (Acoustic Emissions). Zietlow and Labuz (1998) used AE locations pre- and post-peak load to show that the IPZ shape and size is a measurable material property (Sub Figs. 9), similar to the Fracture Process Zone (FPZ).

Few studies model the IPZ directly. Fakhimi et al. (2002) performed an experimental test on a biaxially loaded specimen containing a circular opening. In addition, Fakhimi et al. (2002) used a 2D DEM to model the same biaxial test and compared experimentally collected acoustic emission locations to DEM microcrack locations. Fakhimi et al. (2002) found that the 2D DEM model microcrack cloud thickness was similar to the experimentally observed AE cloud. Another study by Wang et al. (2012) used finite elements to investigate the development of the FPZ around a circular opening in rock. Heterogeneity was addressed with a "homogenous index" (Chun'an Tang, 1997), and acoustic emissions were simulated by recording the released energy of finite elements. Wang et al. (2012) observed an increase of AE cloud width with increasing heterogeneity (decreasing homogenous index) and determined a qualitative agreement with experimental observations.

DEM lends itself well to the simulation of AE activity since broken bonds are analogous to microcracks. Hazzard and Young (2000) and Hazzard and Young (2002) introduced methods for modeling AE within PFC DEM software. Many studies extended and validated the methodology by comparing numerical and experimental Guttenberg-Richter b-values, refining energy calculations, and generating synthetic seismograms (Hazzard and Damjanac, 2013; Khazaei et al., 2015, 2016; Lisjak et al., 2013; Zhang et al., 2017). In all cases, compressive tests yield clouds of simulated AE that compare well to experimental AE observations. Meanwhile, contrary to experimental observations, tensile tests generally produce clean fractures with very few (if any) broken bonds in regions surrounding the rupture (Cai and Kaiser, 2004; Mahabadi et al., 2009). These "clean" fractures are likely due to the typical uniform distribution of particle sizes and the corresponding skewed distribution of bond strengths of traditional DEM. In the cases where heterogeneity is considered, the DEM interaction stiffnesses are stochastically distributed according to macroscopic material property distributions. *Since it is not computationally tractable to model each grain and defect individually, DEM's traditional discretization of space and particle interactions need to be augmented to accommodate for the development of the IPZ.*

1.3 Discrete Element Method

The basic Discrete Element Method (DEM) treats particulate material as an assembly of various sized spheres, each characterized by density and stiffness. Spherical particle interactions and movements are governed by Newton's second law of motion, which enables the integration of sphere positions through time to determine forces. For cohesive assemblies, such as rock, the Bonded Particle Model (BPM) models particle interactions as springs with compressive and tensile strengths (Potyondy and Cundall, 2004). If a spring's strength is exceeded, it is disconnected and the particles interact according to frictional behavior only (or not at all if they are not in contact). The current study employs and modifies Yade open source DEM software (Šmilauer and Chareyre, 2015). Yade's DEM-BPM formulation (Scholtès and Donzé, 2012b) characterizes particle interactions by computing normal (F_n) and shear (F_s) forces based on normal (k_n) and shear (k_s) stiffnesses with a strain evaluation:

$$F_n = k_n \Delta D \tag{1}$$

where ΔD is the difference between the displacement between interacting particles and the predefined equilibrium distance ($\Delta D = D - D_{eq}$). k_n is computed assuming two springs are in serial with lengths equal to the interacting particle radii:

$$k_n = \frac{E_a R_a E_b R_b}{E_a R_a + E_b R_b} \tag{2}$$

and k_s is simply a fraction of k_n, so k_s/k_n is sometimes referred to as the microscopic Poisson's ratio since it has an effect on the lateral/axial deformability of the particle assembly. Since the shear force depends on the orientation of both particles, it is updated incrementally:

$$\Delta F_s = k_s \Delta u_s \tag{3}$$

$$F_s = F_{s,prev} + \Delta F_s \tag{4}$$

where Δu_s is the tangential displacement between particles.

Normal bond strength criterion is defined by Scholtès and Donzé (2012a) as

$$F_{n,max} = -tA_{int} \tag{5}$$

where t is the tensile strength of the bond and $A_{int} = \pi \times \min(R_a, R_b)^2$. The maximum allowable shear force for a given interaction follows a modified Mohr-Coulomb model:

$$F_{s,max} = F_n \tan\phi_b + c_b A_{int} \tag{6}$$

where ϕ_b is a microscopic friction angle and c is the cohesion of the interaction.

Scholtès and Donzé (2012a) also incorporated an interaction range (γ_{int}) to simulate grain interlocking. γ_{int} increases the equilibrium distance, D_{eq}, which allows particles to interact with a greater number of neighboring particles:

$$D_{eq} = \gamma_{int}(R_a + R_b) \tag{7}$$

where R_a and R_b are the radii of interacting particles, and γ_{int} is an interaction range factor. It is important to note that the interaction range should not be high enough to allow interactions that extend across the diameter of another particle:

$$\gamma_{int} < \frac{R_{min} + R_{max}}{R_{max}} \tag{8}$$

2 Methods

2.1 Cathodoluminescence Image Analysis

The current study uses Cathodoluminescence (CL) image analysis to construct an EILD for stochastic augmentation of DEM. CL is particularly useful for such an application since it can be used to distinguish between detrital quartz grains and authigenic quartz (Houseknecht, 1991). Petrographers use the intense Cathodoluminescence (CL) of detrital quartz (due to latex defects and trace cation inclusions) compared to the less intense CL of authigenic cement as a proxy for quartz grain-cement distinction (Fig. 1a). The thresholded grains (Fig. 1b) are further analyzed with ImageJ for particle centroid location $c(x,y)$, particle perimeter coordinates $\mathbf{p}(x,y)$, and particle feret diameter D_{feret} (Rasband, 2012). These grain characteristics are used to detect grain edge interactions as follows:

Particle 1 is the particle of interest, and Particle 2 is the potential interacting neighbor particle. Particle 2 is considered a potential interacting neighbor of Particle 1 when the distance between particle centroids ($d_{centr.}$) is less than the average of the particle feret diameters (D_{feret}):

$$d_{centr.} = \|c_1 - c_2\| < \frac{D_{1,feret} + D_{2,feret}}{2} \tag{9}$$

After the potential neighbors are determined, a point of interest on the Particle 1 perimeter (p_1) is interacting with a point on the Particle 2 perimeter (p_2) if the distance between potential edges (d_{edges}) is less than $D_{1,feret}$ multiplied by a separation factor (s selected a priori as 0.2 for this study):

$$d_{edges} = \|p_1 - p_2\| < sD_{1,feret} \tag{10}$$

The process is repeated for all points on the perimeter of Particle 1. The interacting edge length, l_{edge}, between Particle 1 and Particle 2 is then computed:

$$l_{edge} = \sum_{i=1}^{n} ||P_{1,i} - P_{1,i-1}||_2 \tag{11}$$

where n is the number of points on Particle 1 interacting with Particle 2.

The grain edge interaction detection process was performed for all particles in Fig. 1b. A portion of the interacting edges are shown in Sub Fig. 1b and the edge length distribution is shown in Fig. 2. Finally, a Weibull shape parameter is fit to the edge length distribution by Maximum Likelihood Estimation and Newton Raphson (Appendix A).

2.2 EILD DEM Implementation

The EILD constructed in Sec. 2.1 represents the distribution of interacting edge lengths for a rock specimen. This paper hypothesizes that these interacting edge lengths represent the strength of the grain interactions (i.e. longer interacting edge lengths correspond to higher grain interaction strengths). Such an interpretation can be directly represented in DEM by modifying the interaction strength cross-sectional radii accordingly. Yade's EILD implementation uses a correction factor, α_w (random deviate generated from the EILD (Fig. 3)) to control the DEM interaction area (A_{int}):

$$A_{int} = \alpha_w \times \min(R_a, R_b)^2 \pi \tag{12}$$

Thus, α_w probabilistically weakens or strengthens a bond according to CL microstructure observations. In this way, α_w introduces natural heterogeneities and grain structure into a uniformly distributed DEM packing. The corresponding tensile strength distributions for various Weibull shape parameters are shown in Fig. 4.

2.3 Acoustic Emission simulation in DEM

The current study simulates AE by adopting methodology presented by Hazzard and Young (2000) and Hazzard and Damjanac (2013). Numerically simulated AE events are simulated by assuming each broken DEM bond (or cluster of broken bonds) represents an event location. Additionally, the associated system strain energy change represents the event magnitude. Once a bond breaks, the strain energies (E_i) are summed for all intact bonds within a predefined radius:

$$E_i = \frac{1}{2}\left(\frac{F_n^2}{k_n} + \frac{F_s^2}{k_s}\right) \tag{13}$$

$$E_o = \sum_{i}^{N} E_i \tag{14}$$

where F_n, F_s and k_n, k_s are the normal and shear force (N) and stiffness (N/m) components of the interaction prior to failure, respectively. Hazzard and Damjanac (2013) showed that a volume of 2 to 5 particle diameters (λ) captured the strain energy change of the entire system due to the broken bond of interest. Hazzard and Damjanac (2013) also demonstrated the increase of strain energy with increasing time steps in the model. In Yade's implementation, the time window ($tsteps_{max}$) depends

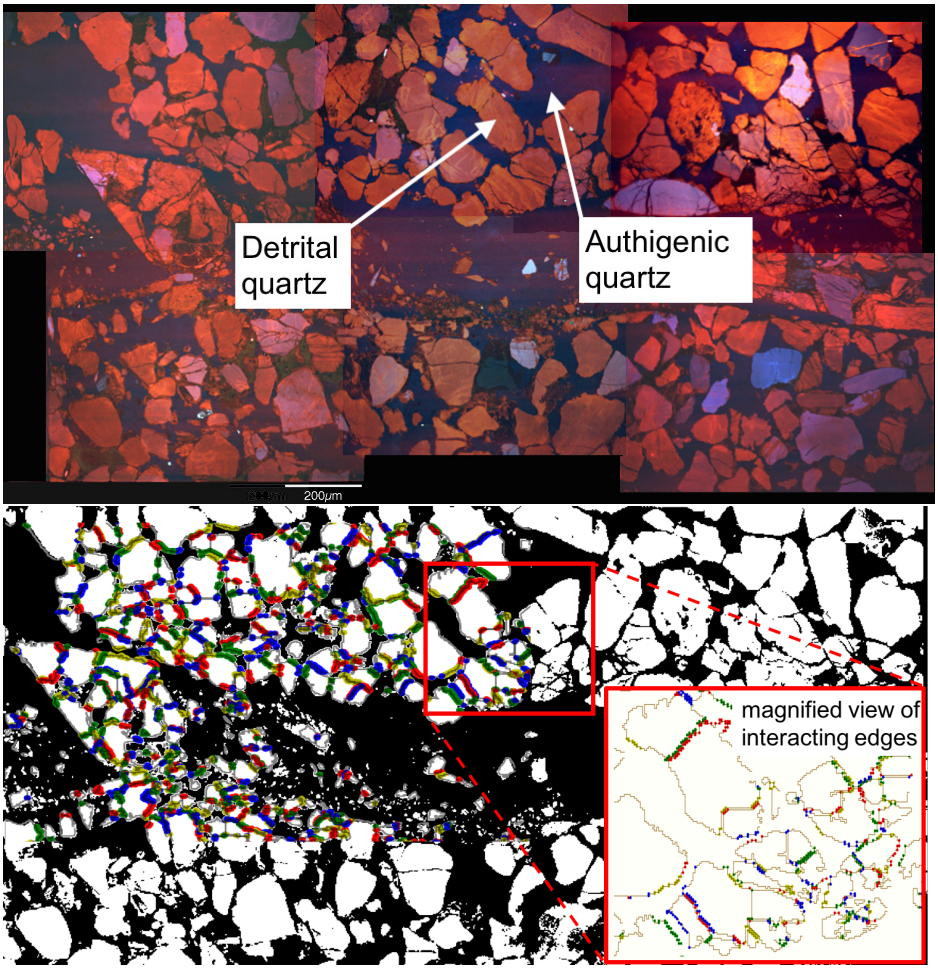

Figure 1. Example of CL scan used to distinguish between detrital (grains) and authigenic (cement) quartz for image analysis (top). Thresholded detrital quartz (white polygons) and samples of detected interacting edges (colored dots) (bottom)

on the P-Wave velocity associated with interacting particle densities (Khazaei et al., 2016):

$$tsteps_{max} = \text{int}\left(\frac{D_{avg}\lambda}{max(v_{p1}, v_{p2})dt}\right) \tag{15}$$

where D_{avg} is the average diameter of the particles comprising the failed event (m), v_{p1} and v_{p2} are the P-Wave velocities (m/s) associated with the interacting particle densities, and dt is the time step of the simulation (seconds/time step).

Yade's AE simulation implementation uses the maximum change of strain energy surrounding each broken bond to estimate the moment magnitude of the AE. As soon as the bond breaks, the total strain energy ($E_o = \sum_i^n E_i$) is computed for the radius (set by the user as no. of avg particle diameters, λ). E_o is used as the reference strain energy to compute $\Delta E = E - E_o$ during subsequent time steps. Finally, $\max(\Delta E)$ is used in the empirical equation derived by Scholz and Harris (2003) to compute the moment magnitude of the acoustic event.

$$M_e = \frac{2}{3}\log \Delta E - 3.2 \tag{16}$$

Since AE waveforms are naturally generated by clusters of microcracks (Lockner, 1993; Scholz and Harris, 2003), broken DEM bonds in Yade are also clustered. Events are clustered if they occur within spatial and temporal windows of other events (similar to the approach presented by Hazzard and Damjanac (2013); Hazzard and Young (2002)). As shown in Fig. 12, the final location of a clustered event is simply the average of the clustered event centroids. Here, the updated reference strain energy is computed by adding the strain energy of the unique interactions surrounding the new broken bond to the original reference strain energy (E_o):

- Original bond breaks, sum strain energy of broken bonds (N_{orig}) within spatial window

$$E_{orig,o} = \sum_{i=1}^{N_{orig}} E_i \tag{17}$$

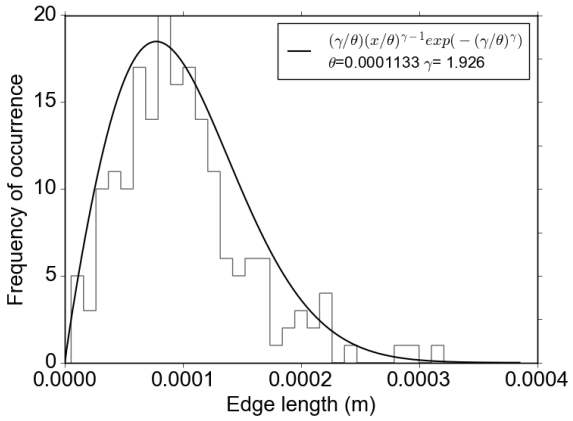

Figure 2. Distribution of interaction edge length

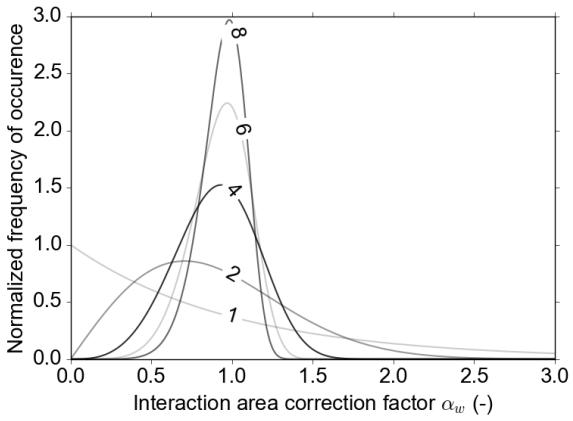

Figure 3. Weibull distributions for varying shape parameters used to generate α_w.

- New broken bond detected within spatial and temporal window of original bond break
- Update reference strain E_o by adding unique bonds (N_{new}) within new broken bond spatial window

$$E_{new,o} = E_{orig,o} + \sum_{i=1}^{N_{new}} E_i \tag{18}$$

This method maintains a physical reference strain energy for the calculation of $\Delta E = E - E_{new,o}$ and depends strongly on the spatial window size. Ultimately, the clustering increases the number of larger events, which yields more comparable b-values of the Guttenberg Richter curve (Hazzard and Damjanac, 2013).

2.4 Three Point Bending Test

The current study validates the EILD-augmented DEM model by comparing numerical and experimental three point bending test results (Zietlow and Labuz, 1998). Both numerical and experimental specimens measure 80 mm x 240 mm x 40 mm and are loaded at the top middle and restrained at both ends as shown in Fig. 5. DEM microproperties are highlighted in Table 1.

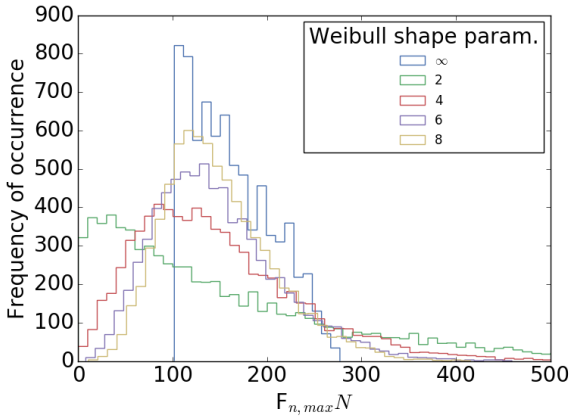

Figure 4. Maximum DEM particle bond tensile strength distributions for varying Weibull shape parameters. Smaller Weibull shape parameters correspond to greater heterogeneity.

Table 1. Numerical specimen DEM microproperties

Micro parameter	Value (DEM)
E_i	50 GPa
k_s/k_n	0.30
ϕ_b	19^o
c_b	40 MPa
t	9 MPa
γ_{int}	1.329
Sphere radius	unif(1.125 mm,1.875 mm)
Sphere density	5000 kg/m^3

The loading piston velocity is constant at 0.03 m/s throughout the test and during failure. Piston load is plotted with respect to piston displacement (specimen deflection). As shown in Fig. 6b, experimental load vs deflection observations are "masked" due to a low machine stiffness, while numerical load vs deflection curves exhibit true material behavior.

3 Results and Discussion

The methodology presented in this paper is implemented into Yade open source software, where it is tested using a Three Point Bending test. First, the EILD-augmented DEM is validated with experimental data gathered from the literature. Next, a micromechanical analysis is performed to gain deeper insight into the effect of heterogeneity on AE event characteristics. Finally, the results are used to demonstrate the distinction between rupture and non-rupture activity.

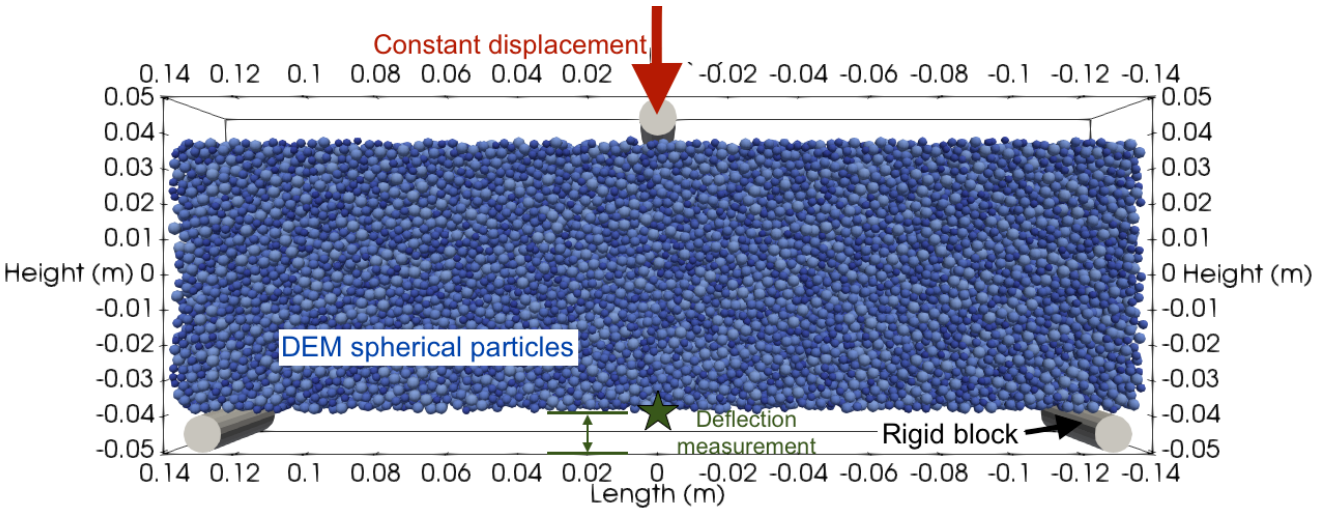

Figure 5. Numerical specimen and three point bending test geometry. Spheres colored by radius (uniform distribution with radius 1.5 mm $\pm$ 0.375 mm.

Three Point Bending test load vs deflection curves follow experimental observations with the peak load occurring between 0.15-0.2 mm deflection (Zietlow and Labuz, 1998). Fig. 6a shows that a Weibull shape parameter of 2 results in lower specimen stiffness, while higher Weibull shape parameters all yield similar stiffnesses. Both low and high Weibull shape parameters yield similar tensile strengths (7-8 MPa). These load vs deflection curves exhibit less pre-failure plasticity and no "snap-back" behavior in comparison to experimental observations (Fig. 6a). These disparities are a result of experimental machine stiffness leading to a "masked" response (Fig. 6b (Labuz and Biolzi, 2007)). Numerically, the "loading machine" maintains infinite stiffness, and therefore yields a truer response as shown in Fig. 6b. Additional load vs deflection disparities can be attributed to rock specimen differences. Zietlow and Labuz (1998) tested quartzite, sandstone, and granite specimens. This study isolated the effect of the Weibull shape parameter, and maintained the same macro parameters of a generic rock.

The AE model described in Sec. 2.3 is validated by magnitude size and distribution. Fig. 8 shows an example of the AE magnitude distribution for a Weibull shape parameter of 4. As shown, the mean event magnitude is -12 and the maximum magnitude is -6.8, which correspond closely to experimentally observed AE magnitudes (Li and Einstein, 2017). The b-value corresponding to the majority of events is 0.84, which is close to 1 as observed by Rao and Lakshmi (2005) and Scholz (1968).

Simulated AE follow the spatial and load-based experimental observations presented by Zietlow and Labuz (1998). Fig. 7 shows how peak load (90-100% max load) AE activity is split with 30-40% occurring between 90-95% max load while the remaining 60-70% occurs between 95-100% max load. Fig. 7 also shows how the AE count decreases with increasing Weibull shape parameter (decreasing heterogeneity), showing how fewer bonds fail as bond strength variation decreases. Numerically simulated spatial AE distributions also match experimentally observed AE spatial distributions; simulated AE events are distributed randomly during 90-95% max load, followed by a concentration of activity around the rupture during 95-100% max load (Fig. 9). Zietlow and Labuz (1998) observed the same random activity during 90-95% max load, followed by the same nucleation of an apparent IPZ during 95-100% max load (Sub Figs. 9). Numerical AE cloud size characteristics also match experimental observations. A Weibull shape parameter of 2 yields an IPZ width of 30-40 mm, while a Weibull shape parameter of ∞ (traditional model) yields an IPZ width of $\leq$ 5 mm. Pre-rupture AE cloud narrows as well, with nearly 0 pre-rupture events occurring in the traditional DEM model. In comparison to laboratory results, Zietlow and Labuz (1998) reported that IPZ widths range from 5 to 30 mm depending on rock type and specimen dimensions (Sub Figs. 9). Experimental IPZ AE activity is confined within the AE sensor array at the base of the rupture (Sub Figs. 9) and any AE activity beyond the array cannot be resolved to less than 2 cm (or not resolved at all (Zietlow and Labuz, 1998)). Despite this experimental shortcoming, both experimental and numerical ruptures track through the center of the IPZ AE cloud (Sub Figures 9 and Fig. 10b). Any disparities between numerical and experimental AE counts/locations are likely caused by the laboratory piezometric transducer threshold limitations, triangulation uncertainties, and unique rock specimen macro behaviors. In particular, a lack of available data prevented careful calibration of the numerical rock specimen to various tensile/compressive tests of each rock specimen presented in Zietlow and Labuz (1998). Many of the behaviorally descriptive DEM microparameters, such as interaction range, bond strengths, and stiffnesses, will impact

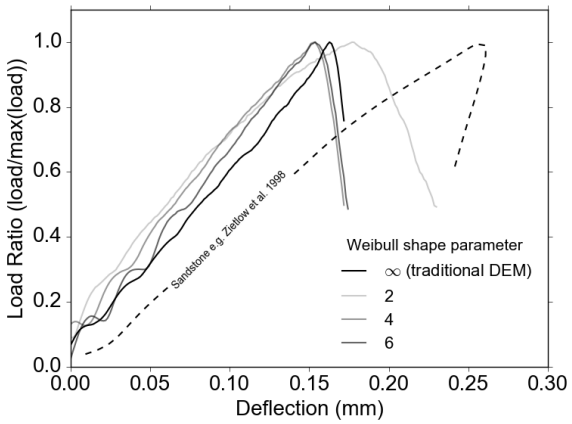

a)

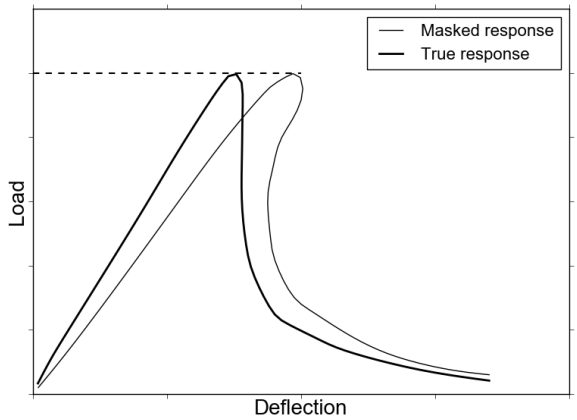

b)

Figure 6. a) Load as a function of deflection for numerical three point bending test for various Weibull shape parameters. Experimental three point bending test data collected by Zietlow and Labuz (1998). b) Masked and true failure curves for infinite and finite laboratory loading machine stiffnesses (Labuz and Biolzi, 2007)

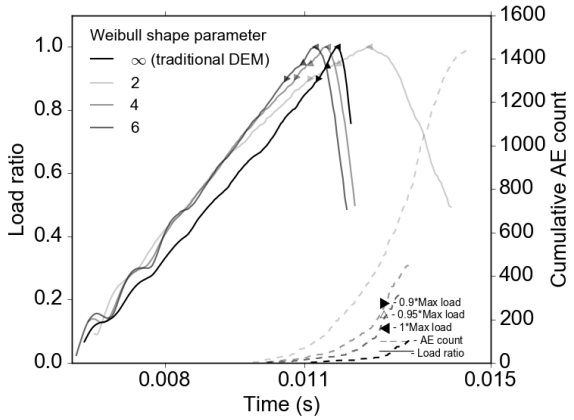

Figure 7. Load and AE count as a function of time for numerical three point bending tests.

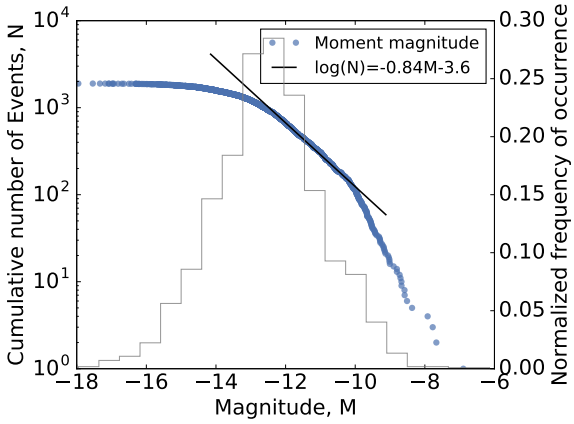

Figure 8. Numerical model AE magnitude distribution (Weibull, shape param.=4)

the spatial and load-based AE distribution. It is important to note that the results presented here demonstrate the influence of the Weibull shape parameter on the spatial and load-based distributions of simulated AE activity in a DEM.

The simulated AE magnitudes enable further investigation of larger rupture AE events and smaller damage AE events (Fig. 10a). For a Weibull shape parameter of 4, the largest event (M-6.14) is located at the center of the rupture. AE magnitude decreases as the AE event location moves away from the rupture and into the damaged region of the specimen (Fig. 10b). The rupture events are distinguished by their number of constituent clustered interactions and magnitude. Fig. 11a-13a show how the largest AE events comprised of more than 10 bonds are focused along a well defined rupture plane, despite an increase of heterogeneity and IPZ width. However, an increase of heterogeneity does correspond to a more distributed release of energy along the rupture plane. Nineteen events comprised of 10 interactions occurred along the rupture plane for the most heterogeneous specimen (Fig. 13). The largest event registered at M-7.87 and was comprised of 28 interactions. At the other end of the spectrum, the least heterogeneous specimen exhibited the sharper release of energy through fewer events (Fig. 11). Five events comprised of 10 interactions occurred along the rupture plane for the least heterogeneous specimen. The largest event registered at M-6.49 and was comprised of ca. 400 interactions. Between the two heterogeneity extremes, a numerical specimen exhibiting the same IPZ width as a Sioux Quartzite exhibited greater rock engagement than the heterogeneous specimen, but also the pronounced sharp release as the homogenous specimen. Twelve events comprised of 10 interactions occurred along the rupture plane (Fig. 12), with the largest event registering at M-6.14 comprised of ca. 300 interactions. For all specimens, the events comprised of 10 interactions exhibited a linear relationship with their event magnitudes. Below this threshold, the activity extends beyond the rupture and into the IPZ, and

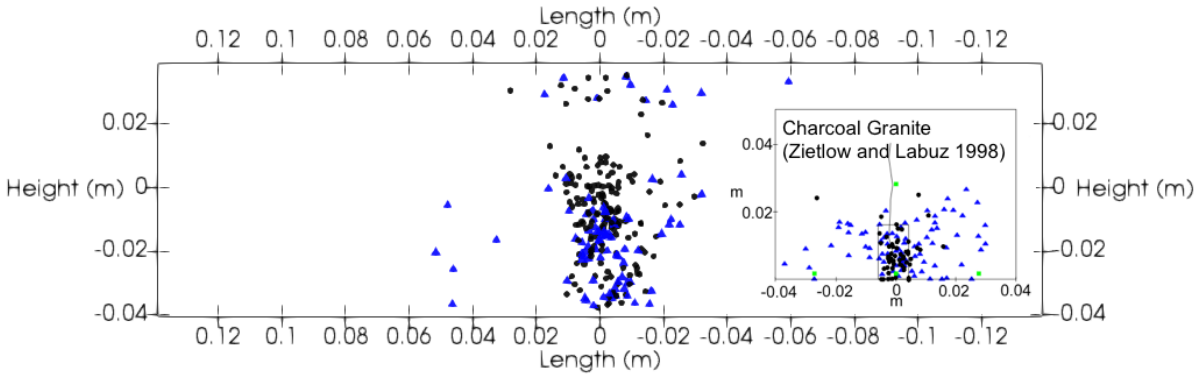

a)

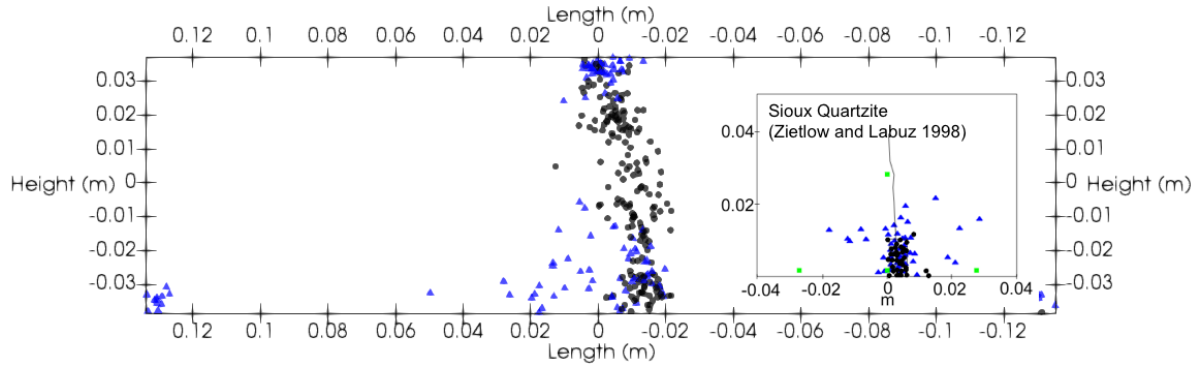

b)

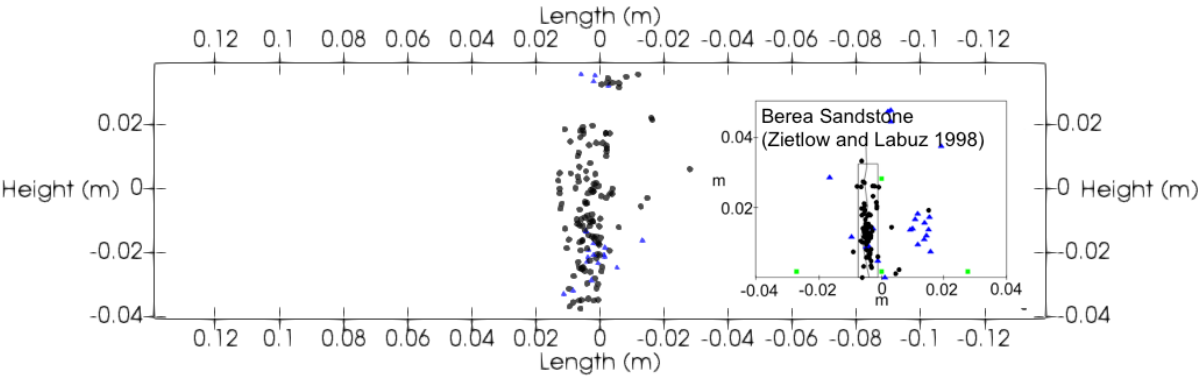

c)

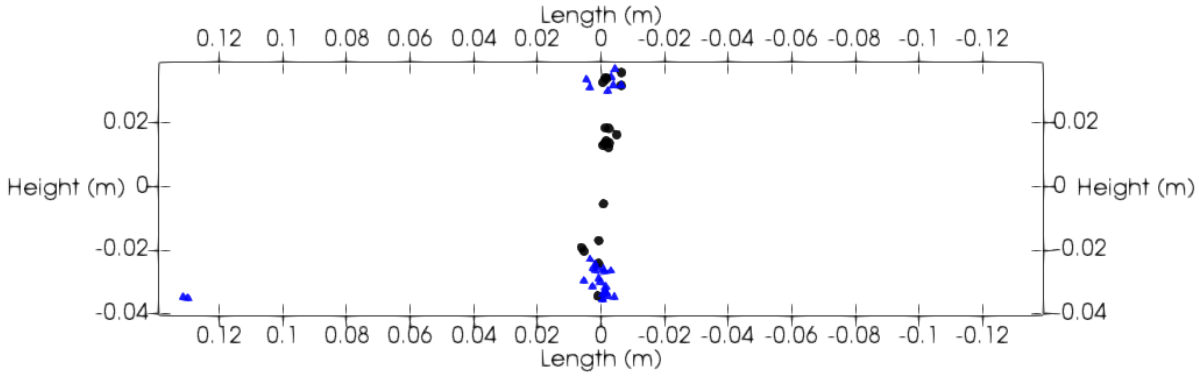

d)

Figure 9. AE distribution for numerical three point bending test (Weibull, shape parameter = a) 2, b) 4, c) 6 d) ∞). Blue triangles represent AE activity between 90-95% max load. Black circles represent AE activity between 95-100% max load. Comparable experimental results shown as sub-figures (Zietlow and Labuz, 1998). Green squares within sub-figures represent the transducer array used by Zietlow and Labuz (1998).

then extends beyond the IPZ and into the pre-failure activity. Thus, for these specimens, the rupture AE activity is easily distinguished from damaged rock AE activity by specifying a threshold of 10 for the number of constituent interactions. Results indicate that large AE events located along the rupture release more energy from larger rock volumes. This intuitive observation provides insight into the numerical specimen behavior. As Sec. 2.3 describes, the event magnitude depends on the *change* of strain energy in bonds surrounding the event. Further, the method clusters interactions (due to spatial and temporal proximities), by increasing the reference strain energy. In other words, new bonds actually *decrease* the change of strain energy value and therefore the AE magnitude. *It follows that the event magnitude can only increase if a truly large material strain energy change occurs over a several grain spatial scale and a P-Wave velocity time scale.* The break down of true heterogenous rock samples may follow a similar spatial/temporal defect coalescence during the generation of large AE rupture events. Meanwhile, small events located beyond the IPZ may be discounted as non-rupture events, instead they are indicative of a damaged volume within the material. These findings enable the distinction between large rupture events at the center of the IPZ and non-rupture AE activity occurring in the damaged volume surrounding the rupture.

4 Conclusion

The methodology presented in this paper aims to improve rock fracture modeling and relieve the computational challenge of modeling rock heterogeneities by augmenting traditional DEM with a physically constructed grain edge-interaction-length distribtuion (EILD). The method simulates naturally occurring heterogeneities, such as microcracks and misshapen grains, by stochastically strengthening and weakening DEM bonds according to the EILD. The method is validated by comparing pre- and post-failure AE locations for numerical and experimental three point bending tests. Similar to experimental observations, a clear IPZ develops within the EILD-aumgented model. As the Weibull shape parameter decreases, the IPZ width increases. Thus, the variation of bond strengths artificially imposes locally "tough" regions and stochastically distributed "microdefects" that arrest and redirect microcracks, respectively. The microcracks occur within some pre-rupture volume (sized depending on EILD variation) and ultimately coalesce to generate AE activity along the rupture. In comparison to the traditional DEM model, the EILD-augmented model is capable of using a physically constructed EILD to simulate various amounts of rock heterogeneity, while traditional DEM fails to capture the experimentally observed rock engagement prior to and following failure.

The analysis presented in this paper aims to provide deeper insight into the role of rock heterogeneities on the rupture process. Results show that larger AE events are located directly along the rupture and their magnitudes are linearly related to their number of constituent interactions. Meanwhile, smaller AE events correspond to failure of weak heterogeneities beyond the rupture. These observations lead to the development of a rupture event threshold to distinguish between larger rupture AE events and smaller damage AE events. Such a distinction enables the direct observation of the rupture via AE activity, even within the wider IPZ zone. Further analysis may be performed to better understand the relationship between grain scale heterogeneties and micromechanical microccrack coalescence for various rock types at different stress/strain states. This analysis may also be extended for comparison with existing continuum damage models.

In summary, this paper outlines the addition of a physically grounded source of rock heterogeneity into DEM. The value of the so-called "EILD" is demonstrated by comparing the numerically and experimentally collected pre- and post-failure AE activity during a three point bending test. After the model is validated, it is used to characterize and distinguish rupture AE activity from damage AE activity within the IPZ. Other uses for the EILD-augmented model include the validation/improvement of existing continuum damage models and understanding the relationship between grain scale heterogeneities and microcrack coalescence at various stress/strain states.

Acknowledgements

This research was partially funded by Dr. Ingrid Tomac and the University of California, San Diego. I want to thank the Yade community for on-going development/technical support and Dr. Ingrid Tomac for helpful comments.

References

Alava, M. J., Nukala, P. K., and Zapperi, S. (2006). Statistical models of fracture. *Advances in Physics*, 55(3-4):349–476.

Berkovits, A. and Fang, D. (1995). Study of fatigue crack characteristics by acoustic emission. *Engineering Fracture Mechanics*, 51(3).

Boyce, G. M., Mccabe, W. M., and Koerner, R. M. (1981). Acoustic Emission Signatures of Various Rock Types in Unconfined Compression. *Geotechnical Engineering Practice*, pages 142–154.

Buxton, G. A., Care, C. M., and Cleaver, D. J. (2001). A lattice spring model of heterogeneous materials with plasticity. *Modelling and Simulation in Materials Science and Engineering*, 9:485–497.

Cai, M. and Kaiser, P. (2004). Numerical simulation of the Brazilian test and the tensile strength of anisotropic rock and rocks with pre-existing cracks. *Int. J. Rock Mech. Min. Sci. & Geomech. Abstr*, 41(3):1–6.

Chun'an Tang (1997). Numerical simulation of progressive rock failure and associated seismicity. *International journal of rock mechanics and mining sciences & geomechanics abstracts*.

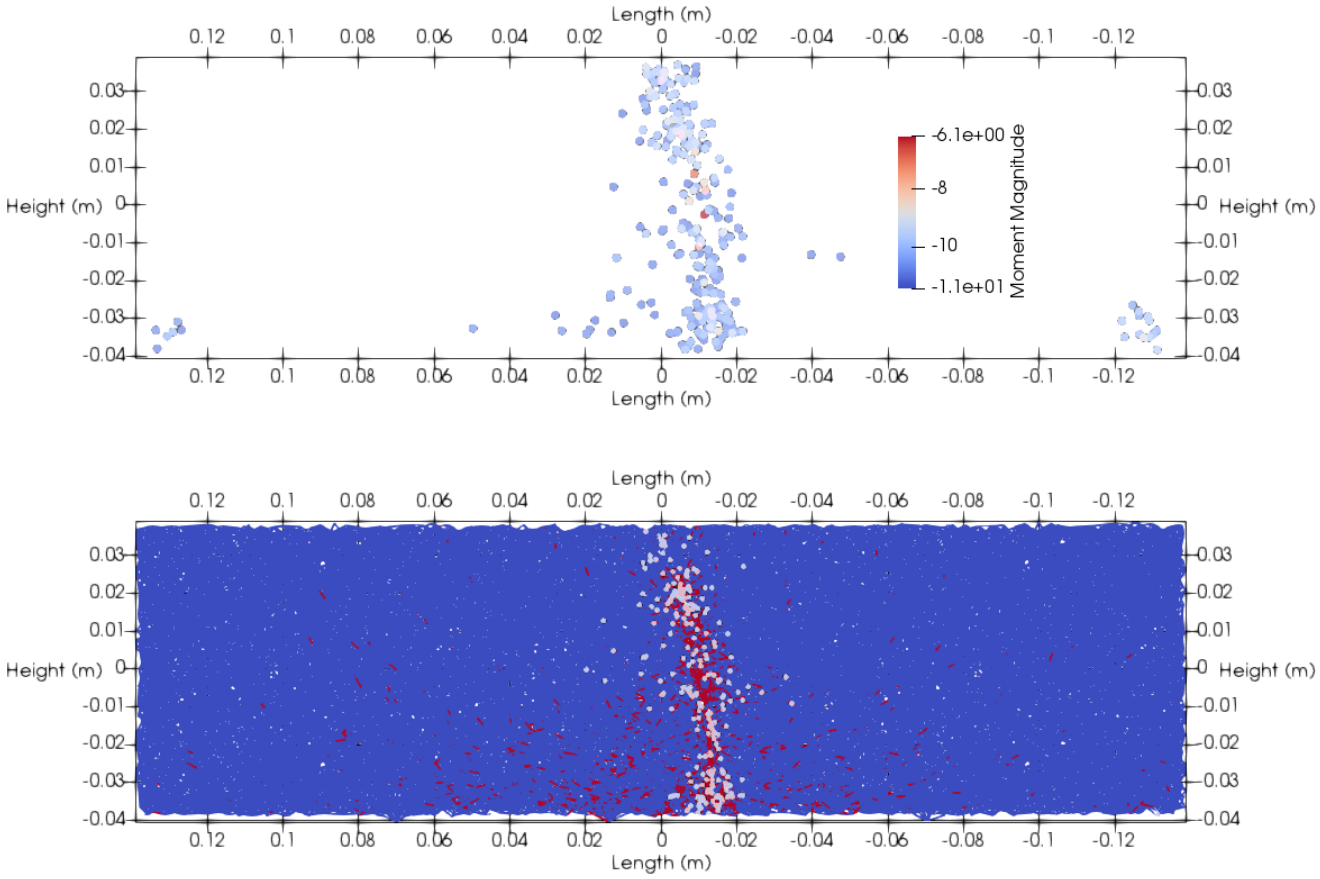

Figure 10. Numerical model spatial AE magnitude distribution (Weibull shape param.=4) (top). Rupture plane with respect to IPZ AE activity (95-100% max load). Broken bonds (red), intact bonds (blue), IPZ AE events (white circles) (Weibull,shape param. =4) (bottom)

a)

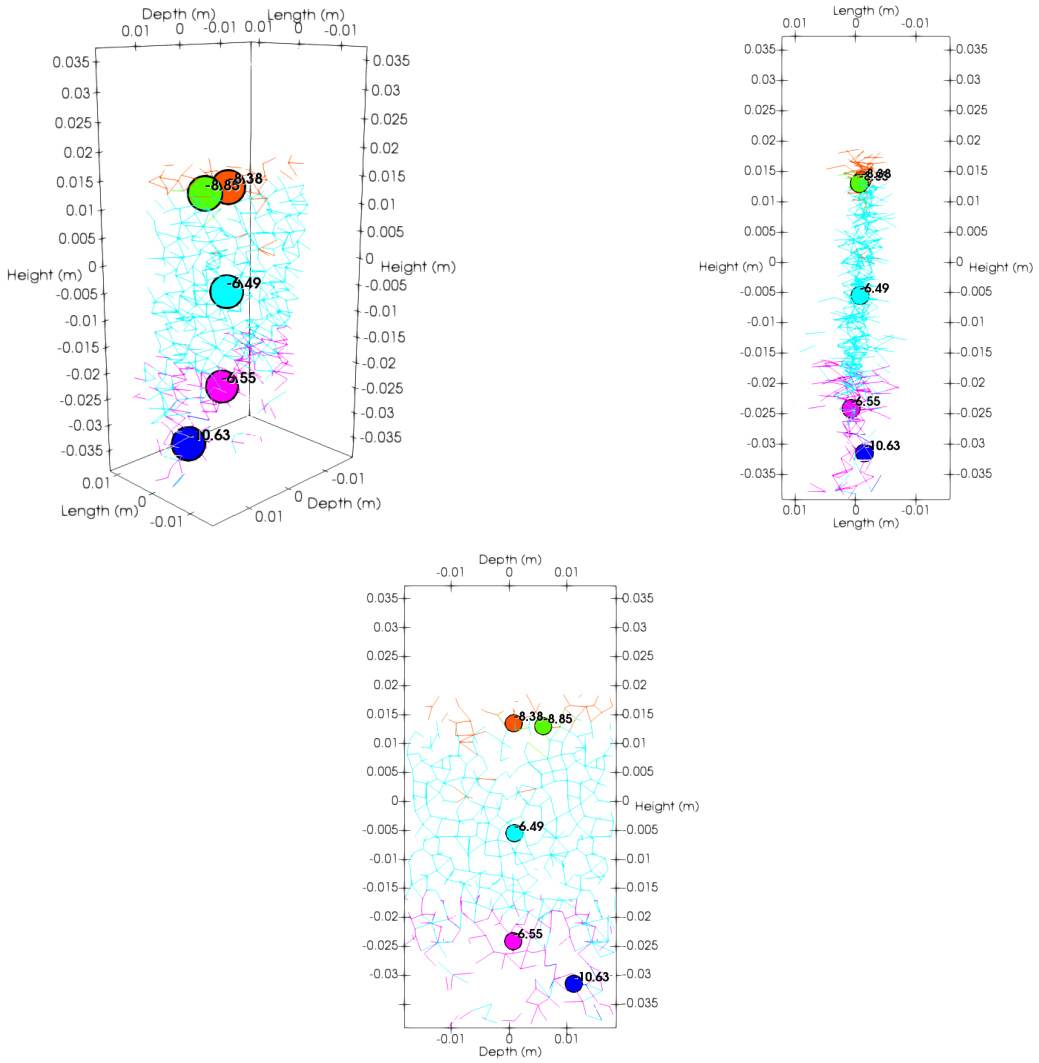

b)

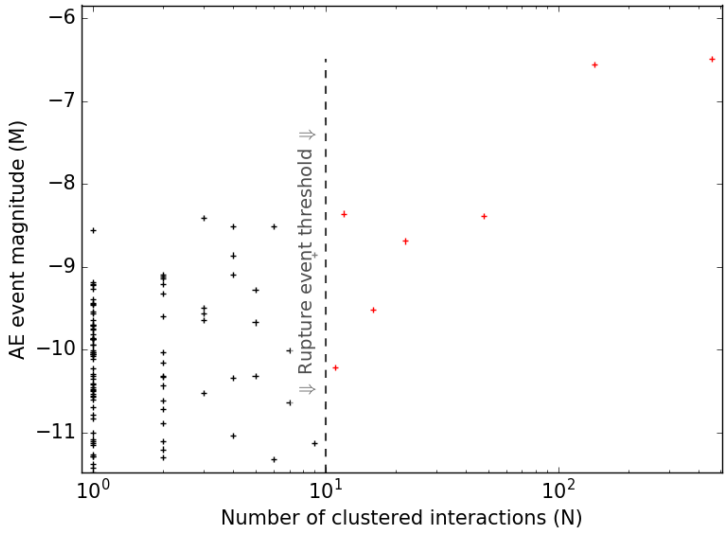

Figure 11. a) Failure plane AE events (colored circles) comprised of $\geq$10 clustered broken bonds (colored lines) b) Event magnitudes as a function of number of clustered interactions (Weibull, shape param.=∞)

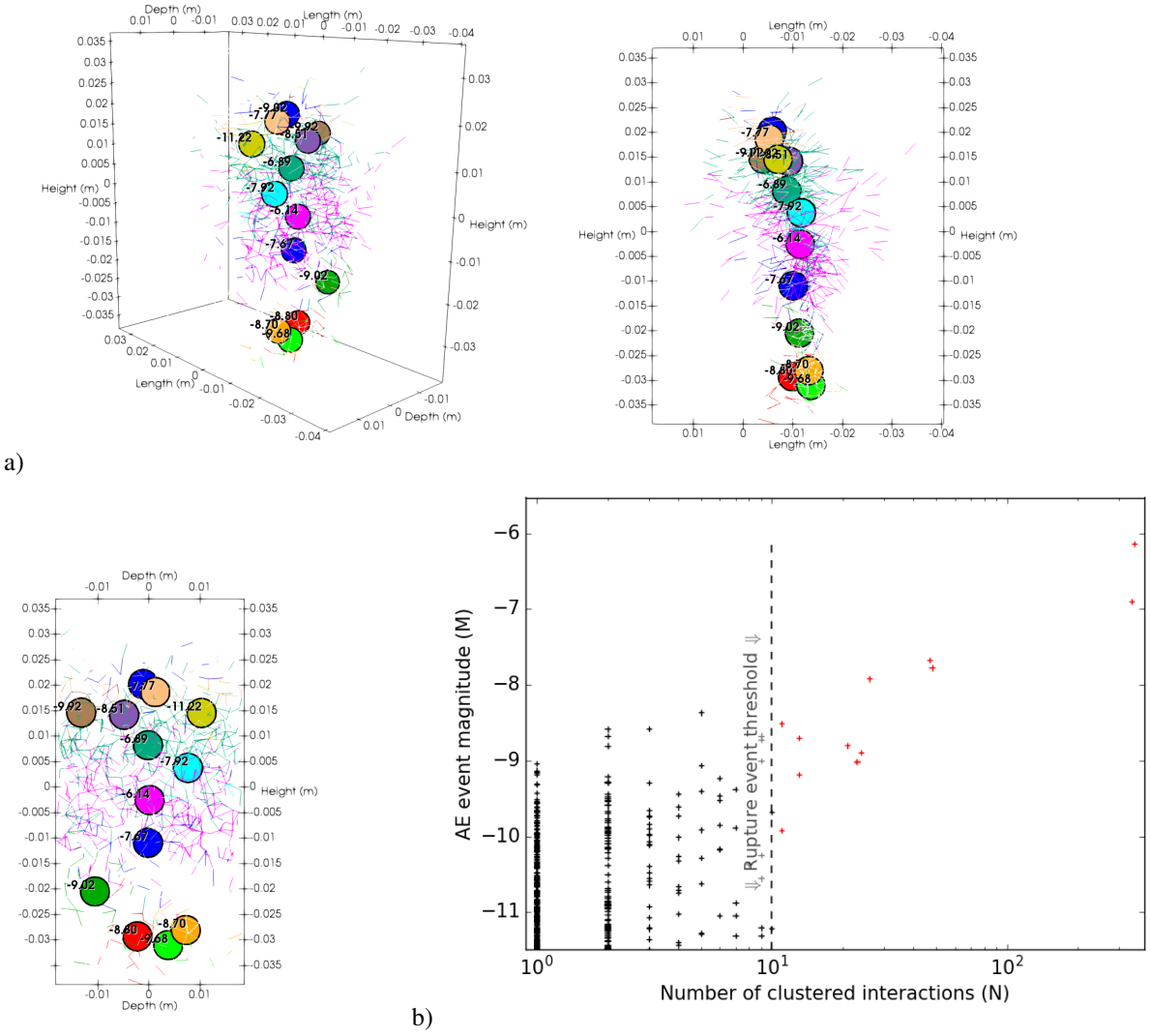

Figure 12. a) Failure plane AE events (colored circles) comprised of ≥10 clustered broken bonds (colored lines) b) Event magnitudes as a function of number of clustered interactions (Weibull, shape param.=4)

a)

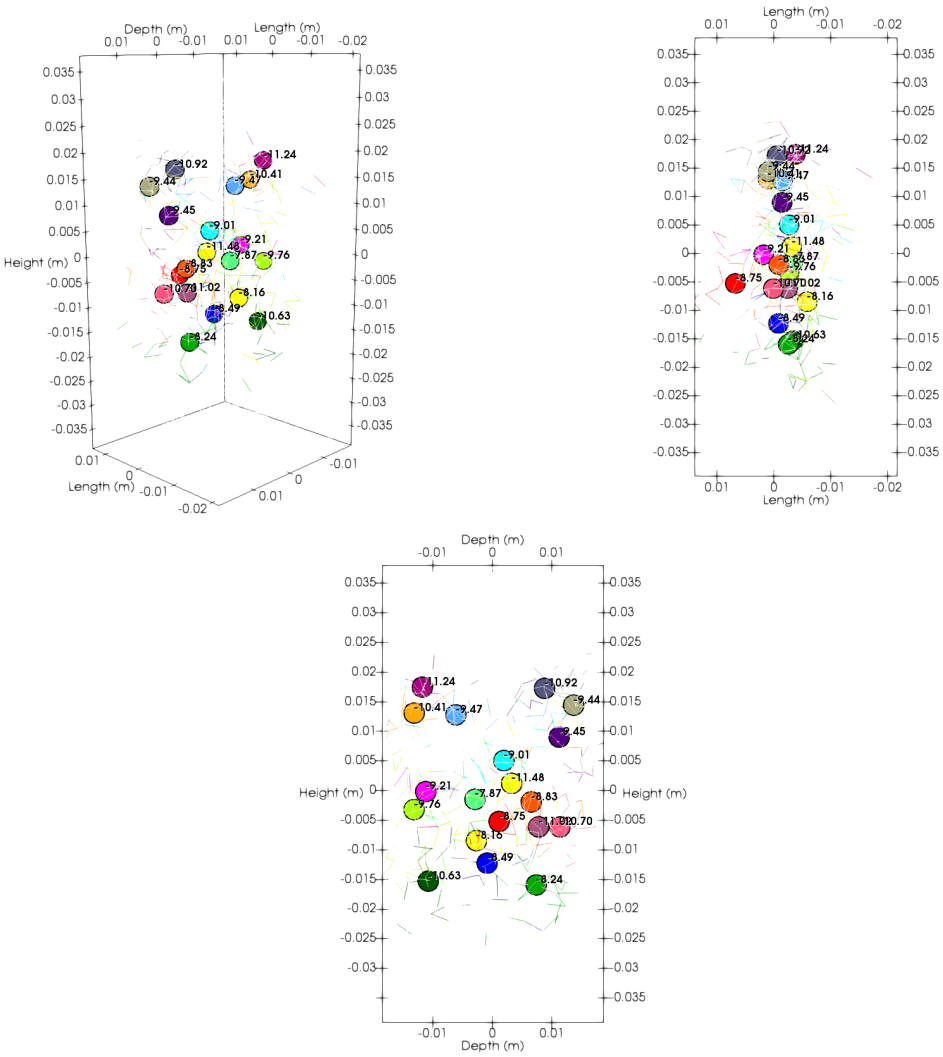

b)

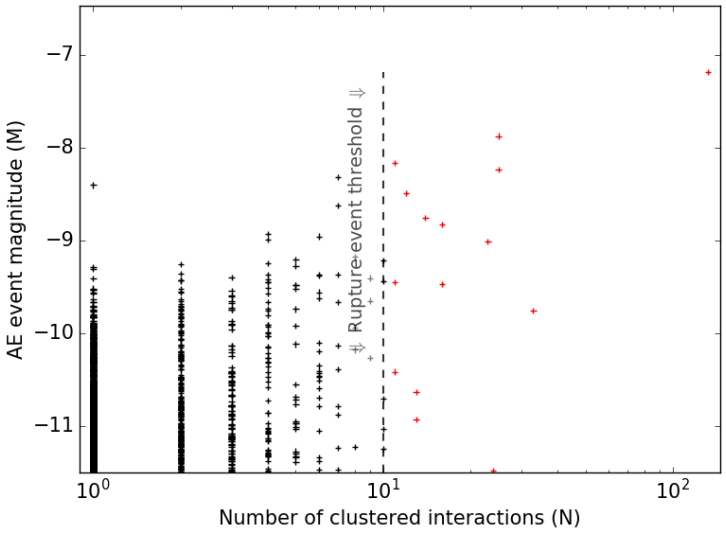

Figure 13. a) Failure plane AE events (colored circles) comprised of $\geq$10 clustered broken bonds (colored lines) b) Event magnitudes as a function of number of clustered interactions (Weibull, shape param.=2)

Eitzen, D. and Wadley, N. (1984). Acoustic Emission : Establishing the Fundamentals. *Journal of Research of the National Bureau of Standards*, 89(1):75–100.

Fakhimi, A., Carvalho, F., Ishida, T., and Labuz, J. (2002). Simulation of failure around a circular opening using CWFS model. *International Journal of Rock Mechanics and Mining Sciences*, 39:507–515.

Garboczi, E. J. and Day, A. R. (1995). An algorithm for computing the effective linear elastic properties of heterogeneous materials: Three-dimensional results for composites with equal phase poisson ratios. *Journal of the Mechanics and Physics of Solids*, 43(9):1349–1362.

Godin, N., Huguet, S., Gaertner, R., and Salmon, L. (2004). Clustering of acoustic emission signals collected during tensile tests on unidirectional glass/polyester composite using supervised and unsupervised classifiers. *NDT and E International*, 37(4):253–264.

Hazzard, J. and Young, R. (2000). Simulating acoustic emissions in bonded-particle models of rock. *International Journal of Rock Mechanics and Mining Sciences*, 37(5):867–872.

Hazzard, J. F. and Damjanac, B. (2013). Further investigations of microseismicity in bonded particle models. *3rd International FLAC/DEM Symposium*, pages 1–11.

Hazzard, J. F. and Young, R. P. (2002). Moment tensors and micromechanical models. *Tectonophysics*, 356:181–197.

Hazzard, J. F. and Young, R. P. (2004). Dynamic modelling of induced seismicity. *International Journal of Rock Mechanics and Mining Sciences*, 41(8):1365–1376.

Houseknecht, D. (1991). Use of cathodoluminescence petrography for understanding compaction, quartz cementation, and porosity in sandstones. *Luminiscence Microscopy: Quantitative and Qualitative Aspects*, pages 59–66.

Khazaei, C., Hazzard, J., and Chalaturnyk, R. (2015). Damage quantification of intact rocks using acoustic emission energies recorded during uniaxial compression test and discrete element modeling. *Computers and Geotechnics*, 67(2015):94–102.

Khazaei, C., Hazzard, J., and Chalaturnyk, R. (2016). A discrete element model to link the microseismic energies recorded in caprock to geomechanics. *Acta Geotechnica*, 11(6):1351–1367.

Labuz, J. F. and Biolzi, L. (2007). Experiments with rock: Remarks on strength and stability issues. *International Journal of Rock Mechanics and Mining Sciences*, 44(4):525–537.

Labuz, J. F., Cattaneo, S., and Chen, L. H. (2001). Acoustic emission at failure in quasi-brittle materials. *Construction and Building Materials*, 15(5-6):225–233.

Labuz, J. F., Shah, S. P., and Dowding, C. H. (1987). The fracture process zone in granite: evidence and effect. *International Journal of Rock Mechanics and Mining Sciences and*, 24(4):235–246.

Lei, X., Masuda, K., Nishizawa, O., Jouniaux, L., Liu, L., Ma, W., Satoh, T., and Kusunose, K. (2004). Detailed analysis of acoustic emission activity during catastrophic fracture of faults in rock. *Journal of Structural Geology*, 26:247–258.

Lei, X.-L., Kusunose, K., Nishizawa, O., Cho, A., and Satoh, T. (2000). On the spatio-temporal distribution of acoustic emissions in two granitic rocks under triaxial compression: The role of pre-existing cracks. *Geophysical Research Letters*, 27(13):1997–2000.

Li, B. Q. and Einstein, H. H. (2017). Comparison of Visual and Acoustic Emission Observations in a Four Point Bending Experiment on Barre Granite. *Rock Mechanics and Rock Engineering*, 50(9):2277–2296.

Lisjak, A., Liu, Q., Zhao, Q., Mahabadi, O. K., and Grasselli, G. (2013). Numerical simulation of acoustic emission in brittle rocks by two-dimensional finite-discrete element analysis. *Geophysical Journal International*, 195(1):423–443.

Liu, H. Y., Roquete, M., Kou, S. Q., and Lindqvist, P. A. (2004). Characterization of rock heterogeneity and numerical verification. *Engineering Geology*, 72(1-2):89–119.

Lockner, D. A. (1993). The role of acoustic emission in the study of rock fracture. *International Journal of Rock Mechanics and Mining Sciences & Geomechanics Abstracts*, 30(7):883–899.

Lockner, D. A., Byerlee, J. D., Kuksenko, V., Ponomarev, A., and Sidorin, A. (1992). Chapter 1 Observations of Quasistatic Fault Growth from Acoustic Emissions. *International Geophysics*, 51(C):3–31.

Ma, Y. and Huang, H. (2017). Tensile strength calibration in DEM modeling. *American Rock Mechanics Association*.

Mahabadi, O., Grasselli, G., and Munjiza, A. (2009). Numerical modelling of a Brazilian Disc test using the combined finite-discrete element method. In Diederichs, M. and Grasselli, G., editors, *CANUS Rock Mechanics Sumposium*, Toronto.

McLaskey, G. C., Lockner, D. A., Kilgore, B. D., and Beeler, N. M. (2015). A robust calibration technique for acoustic emission systems based on momentum transfer from a ball drop. *Bulletin of the Seismological Society of America*, 105(1):257–271.

Ostoja-Starzewski, M., Sheng, P. Y., and Jasiuk, I. (1994). Influence of random geometry on effective properties and damage formation in composite materials. *J. Engg. Mat. Tech.*, 116(July 1994):384–391.

Potyondy, D. O. and Cundall, P. A. (2004). A bonded-particle model for rock. *International Journal of Rock Mechanics and Mining Sciences*, 41(8):1329–1364.

Rabczuk, T. and Eibl, J. (2006). Modelling dynamic failure of concrete with meshfree methods. *International Journal of Impact Engineering*, 32(11):1878–1897.

Rao, M. V. M. S. and Lakshmi, K. J. P. (2005). Analysis of b -value and improved b -value of acoustic emissions accompanying rock fracture. *Curreent Science*, 89(9):1577–1582.

Rasband, W. (2012). ImageJ. *U. S. National Institutes of Health, Bethesda, Maryland, USA*, page //imagej.nih.gov/ij/.

Scholtès, L. and Donzé, F. V. (2012a). A DEM model for soft and hard rocks: Role of grain interlocking on strength. *Journal of the Mechanics and Physics of Solids*, 61:352–369.

Scholtès, L. and Donzé, F.-V. (2012b). Modelling progressive failure in fractured rock masses using a 3D discrete element method. *International Journal of Rock Mechanics and Mining Sciences*, 52:18–30.

Scholz, C. H. (1968). The frequency-magnitude relation of microfrackturing in rock and its relation to earthquakes. *Seismological Society of America*, 58(1):399–415.

Scholz, C. H. and Harris, R. A. (2003). "The Mechanics of Earthquakes and Faulting - Second Edition" by Christopher H. Scholz. *Seismological Research Letters*, 74(3):333–333.

Sfantos, G. K. and Aliabadi, M. H. (2007). Multi-scale boundary element modelling of material degradation and fracture. *Computer Methods in Applied Mechanics and Engineering*, 196(7):1310–1329.

Shah, K. R. and Labuz, J. F. (1995). Damage mechanism in stressed rock from acoustic emission. *Journal of Geophysical Research*, 100:15527–15539.

Shearer, P. (2009). *Introduction to Seismology*. Cambridge University Press.

Šmilauer, V. and Chareyre, B. (2015). DEM Formulation, Release Yade documentation. *Yade Documentation*, pages 137–160.

Soma, N., Niitsuma, H., and Baria, R. (2002). Reflection technique in time-frequency domain using multicomponent acoustic emission signals and application to geothermal reservoirs. *Distribution*, 67(3):928–938.

Sondergeld, C. H. and Estey, L. H. (1981). Acoustic emission study of microfracturing during the cyclic loading of Westerly granite. *Journal of Geophysical Research*, 86(B4):2915–2924.

Tang, C. and Kaiser, P. (1998). Numerical Simulation of Cumulative Damage and Seismic Energy Release During Brittle Rock Failure—Part I: Fundamentals. *International Journal of Rock Mechanics and Mining Sciences*, 35(2):113–121.

Wang, S. Y., Sloan, S. W., Sheng, D. C., and Tang, C. A. (2012). Numerical analysis of the failure process around a circular opening in rock. *Computers and Geotechnics*, 39(2012):8–16.

Wang, X. L. and Li, J. C. (2014). Simulation of triaxial response of granular materials by modified DEM. *Science China: Physics, Mechanics and Astronomy*, 57(12):2297–2308.

Yang, S. Q., Jing, H. W., and Wang, S. Y. (2012). Experimental investigation on the strength, deformability, failure behavior and acoustic emission locations of red sandstone under triaxial compression. *Rock Mechanics and Rock Engineering*, 45(4):583–606.

Yang, T. H., Tham, L. G., Tang, C. A., Liang, Z. Z., and Tsui, Y. (2004). Influence of heterogeneity of mechanical properties on hydraulic fracturing in permeable rocks. *Rock Mechanics and Rock Engineering*, 37(4):251–275.

Zang, A., Wagner, F. C., Stanchits, S., Dresen, G., Andersen, R., and M.Haidekker (1998). Source analysis of acoustic emission in Aue granite cores under symmetric and asymmetric loads. *Geophysical Journal International*, 135:1113.

Zhang, X.-P., Zhang, Q., and Wu, S. (2017). Acoustic emission characteristics of the rock-like material containing a single flaw under different compressive loading rates. *Computers and Geotechnics*, 83(2017):83–97.

Zietlow, W. K. and Labuz, J. F. (1998). Measurement of the Intrinsic Process Zone in rock using acoustic emission. *Int. J. Rock Mech. Min. Sci.*, 35(3):291–299.

Appendices

A Newton Raphson maximum-likelihood parameter estimation for EILD:

The Weibull distribution is an exponential probability density function (PDF) described by a shape parameter (γ) and scale parameter (θ):

$$\phi = f(x_i|\theta,\gamma) = \left(\frac{\gamma}{\theta}\right)\left(\frac{x}{\theta}\right)^{\gamma-1} exp(-(x/\theta))^{\gamma} \qquad (19)$$

We use the log-likelihood of the PDF for a maximum likelihood parameter estimation:

$$L(\theta,\gamma) = \sum_{i=1}^{n} \ln f(x_i|\theta,\gamma) \qquad (20)$$

all summations from here on are w.r.t x_i from $i = 1$ to n

$$\ln L = n\ln\gamma - n\ln\theta - \sum\left(\frac{x}{\theta}\right)^{\gamma} + (\gamma-1)\sum\ln x \tag{21}$$

$$\frac{d\ln L}{d\gamma} = \frac{n}{\gamma} - n\ln\theta - \sum\left(\frac{x}{\theta}\right)^{\gamma}\ln\frac{x}{\theta} + \sum\ln x = 0 \tag{22}$$

$$\frac{d\ln L}{d\theta} = -\frac{n\gamma}{\theta} + \sum\frac{\gamma\left(\frac{x}{\theta}\right)^{\gamma}}{\theta} = 0 \tag{23}$$

now we solve for θ

$$\theta = \left(\frac{\sum x^{\gamma}}{n}\right)^{\gamma} \tag{24}$$

and plug into $\frac{d\ln L}{d\gamma}$

$$f(\gamma) = \frac{\sum x^{\gamma}\ln x}{\sum x^{\gamma}} - \frac{\sum\ln x}{n} - \frac{1}{\gamma} \tag{25}$$

and the derivative for Newton-Raphson:

$$\frac{df}{d\gamma} = \frac{\sum x^{\gamma}\ln^2 x\sum x^{\gamma} - (\sum x^{\gamma}\ln x)^2}{\sum(x^{\gamma})^2} + \frac{1}{\gamma^2} \tag{26}$$

where γ is solved for iteratively with Newton-Raphson:

$$\gamma = \gamma_o + \frac{f(\gamma)}{\frac{df}{d\gamma}} \tag{27}$$

once γ is obtained, it is used to obtain θ